SPECIAL TOPIC — Smart design of materials and design of smart materials

Lattice thermal conductivity switching via structural phase transition in ferromagnetic VI_3

Chao Wu(吴超)[1,4] and Chenhan Liu(刘晨晗)[1,2,3,†]

[1] *Laboratory of Solid State Microstructures, Nanjing University, Nanjing* 210093, *China*
[2] *Micro- and Nano-scale Thermal Measurement and Thermal Management Laboratory, School of Energy and Mechanical Engineering, Nanjing Normal University, Nanjing* 210023, *China*
[3] *Jiangsu Key Laboratory for Numerical Simulation of Large-Scale Complex Systems, Nanjing Normal University, Nanjing* 210023, *China*
[4] *Jiangsu Key Laboratory for Design and Manufacture of Micro-Nano Biomedical Instruments, School of Mechanical Engineering, Southeast University, Nanjing* 211100, *China*

(Received 16 November 2022; revised manuscript received 10 January 2023; accepted manuscript online 31 January 2023)

The realization of reversible thermal conductivity through ferromagnetic ordering can improve the heat management and energy efficiency in magnetic materials-based devices. VI_3, as a new layered ferromagnetic semiconductor, exhibits a structural phase transition from monoclinic ($C2/m$) to rhombohedral ($R\bar{3}$) phase as temperature decreases, making it a suitable platform to investigate thermal switching in magnetic phase transition materials. This work reveals that the thermal switching ratio of VI_3 can reach 3.9 along the a-axis. Mechanical properties analysis indicates that the $C2/m$ structure is stiffer than the $R\bar{3}$ one, causing the larger phonon velocity in $C2/m$ phase. Moreover, due to the fewer phonon branches in $C2/m$ phase, the number of phonon–phonon scattering channels in $C2/m$ phase is smaller compared to that of $R\bar{3}$ phase. Both the larger phonon velocity and the longer phonon lifetime lead to larger lattice thermal conductivity in $C2/m$ phase. This study uncovers the mechanical and thermal properties of VI_3, which provides useful guides for designing magnetic materials-based devices such as thermal switch.

Keywords: thermal switching, ferromagnetic ordering, phonons

PACS: 65.80.Ck, 77.80.Fm, 77.80.B– **DOI:** 10.1088/1674-1056/acb764

1. Introduction

Thermal switch, which provides an opportunity for controlling heat flow flexibly, has attracted tremendous attention.[1–5] The performance of thermal switch is estimated by the switching ratio κ_{on}/κ_{off}, where κ_{on} and κ_{off} are the highest and the lowest thermal conductivity during the switching process, respectively.[6,7] Thermal switching can be realized in ferroelectric, ferromagnetic, and ferroelastic materials.[8–12] For example, a $\sim 11\%$ change in thermal conductivity was observed in $Pb(Zr_{0.3}Ti_{0.7})O_3$ thin films because of the variations in the ferroelectric domain density induced by an electric field.[13] Liu *et al.*[14] also reported that the thermal conductivity of polycrystalline $Cu_{2-x}Se$ can vary by 77% due to the temperature induced phase transition. Much larger switching ratio of $\sim 8\times$ was achieved in polyethylene nanofibers due to the structural phase transition.[15] Similarly, Lu *et al.*[16] also reported a switching ratio of $\sim 10\times$ in $SrCoO_x$ by employing ionic liquid gating to cause the structural phase transitions. Theoretically, Liu *et al.*[17] predicted that the thermal conductivity decreases by 5.8 times with the structure transforming from $P4mm$ to Pm phase. Moreover, Wang *et al.*[8] proposed that the maximum switching ratio of $PdSe_2$ can reach an order of magnitude by strain-driven structural phase transition. As discussed above, phase transition plays a vital role in causing large switching ratio and phase transition can be controlled by various methods such as strain, electric field, and temperature.

In addition to ferroelectric and ferroelastic materials, ferromagnetic materials are also potential candidates for switchable thermal conductivity. VI_3, which belongs to ferromagnetic van der Waals (vdW) materials, has been synthesized successfully.[18–20] Like layered chromium trihalides, VI_3 undergoes a structural transition from monoclinic phase with space group $C2/m$ to rhombohedral one with space group $R\bar{3}$ as the temperature decreases to 79 K.[19] Moreover, several works observed that VI_3 exhibits long-range ferromagnetic ordering and behaves insulating below 50 K.[19,20] Tian *et al.*[19] reported that VI_3 undergoes an obvious structural phase transition from monoclinic to rhombohedral at 79 K, while Kong *et al.*[20] found that it experiences a subtle structural transition without changes in symmetry space group. Further theoretical and experimental studies are needed to understand this contradiction.

In the current work, the dynamic stability of different structures and thermal switching in VI_3 are systematically investigated with first-principles calculations. The low-temperature structure ($R\bar{3}$ phase) of VI_3 is optimized with spin (ferromagnetic, FM) or without spin (nonmagnetic, NM) po-

†Corresponding author. E-mail: chenhanliu@njnu.edu.cn

© 2023 Chinese Physical Society and IOP Publishing Ltd

larization. The imaginary frequency appeared in NM $R\bar{3}$ phase implies that the lattice structure of $R\bar{3}$ phase without FM ordering is dynamically unstable. For the high-temperature structure with space group $C2/m$, there is no imaginary frequency when the calculations exclude spin polarization. Therefore, the high-temperature phase of VI_3 could prefer to the NM $C2/m$ structure. Although the reversibility of phase transition driven by temperature in VI_3 has not been demonstrated in this work, the temperature is a highly controllable and reversible tuning knob to drive the phase transition.[21,22] Moreover, cooling triggered phase transition from $C2/m$ to $R\bar{3}$ phase in VI_3 has been demonstrated experimentally,[19,20] thus, we believe the phase dependent thermal conductivity in VI_3 can realize the thermal switching, i.e., reversible modulation of thermal conductivity. Furthermore, the mechanical properties of FM $R\bar{3}$ and NM $C2/m$ phases are calculated and show that the $C2/m$ phase is stiffer than the $R\bar{3}$ one. This leads to larger phonon group velocity and longer phonon lifetime in $C2/m$ phase and then results in larger thermal conductivity. Thermal switching ratio of VI_3 can reach to 3.9 along the a-axis at the phase transition temperature of 50 K. Moreover, the longer phonon lifetime caused by smaller phonon scattering channels also contributes to the larger thermal conductivity in $C2/m$ phase.

2. Methods

For the first-principles calculations, the package VASP was employed and the Perdew–Burke–Ernzerhof of generalized gradient approximation (GGA) was chosen as the exchange–correlation functional.[23] The Γ-centered $\boldsymbol{k}$-mesh was set as $11\times11\times5$ for $R\bar{3}$ phase ($11\times5\times11$ for $C2/m$ phase) to simulate the Brillouin zone in the total energy calculation and structural optimization. To introduce the vdW interactions into VI_3, we imposed the density functional dispersion correction method of Grimme (DFT-D3)[24] in all calculations. The tolerances for structural optimization were set as the difference in atomic force being within 10^{-3} eV/Å. In order to calculate Young's modulus of VI_3, a larger energy cutoff of 600 eV was chosen. First, the elastic tensor was determined by performing six finite distortions of the lattice, then the elastic constants was obtained based on the previous elastic tensor and the strain–stress relationship.[25] Finally, the Young's moduli of VI_3 were derived from elastic constants C_{ij} metrics through a series of formulas.[26,27]

For $R\bar{3}$ phase:

$$B_{\rm V}=\frac{2}{9}\left(C_{11}+C_{12}+\frac{C_{33}}{2}+2C_{13}\right), \tag{1}$$

$$G_{\rm V}=\frac{1}{30}(7C_{11}-5C_{12}+12C_{44}+2C_{33}+4C_{13}), \tag{2}$$

$$B_{\rm R}=\frac{[(C_{11}+C_{12})C_{33}-2C_{13}^2]}{(C_{11}+C_{12}+2C_{33}-4C_{13})}, \tag{3}$$

$$G_{\rm R}=\frac{5}{2}\left\{\frac{[(C_{11}+C_{12})C_{33}-2C_{13}^2]C_{44}C_{66}}{3B_{\rm V}C_{44}C_{66}+[(C_{11}+C_{12})C_{33}-2C_{13}^2](C_{44}+C_{66})}\right\}. \tag{4}$$

For $C2/m$ phase:

$$\begin{aligned}B_{\rm R}=\;&\Omega\big[a(C_{11}+C_{22}-2C_{12})+b(2C_{12}-2C_{11}-C_{23})\\&+c(C_{15}-2C_{25})+d(2C_{12}+2C_{23}-C_{13}-2C_{22})\\&+2e(C_{25}-C_{15})+f\big]^{-1},\end{aligned} \tag{5}$$

$$\begin{aligned}G_{\rm R}=\;&15\Big\{4\big[a(C_{11}+C_{22}+C_{12})+b(C_{11}-C_{12}-C_{23})\\&+c(C_{15}+C_{25})+d(C_{22}-C_{12}-C_{23}-C_{13})\\&+e(C_{15}-C_{25})+f\big]/\Omega+3\left[\frac{g}{\Omega}+\frac{C_{44}+C_{66}}{C_{44}C_{66}-C_{46}^2}\right]\Big\}^{-1},\end{aligned} \tag{6}$$

$$a=C_{33}C_{55}-C_{35}^2, \tag{7}$$

$$b=C_{23}C_{55}-C_{25}C_{35}, \tag{8}$$

$$c=C_{13}C_{35}-C_{15}C_{33}, \tag{9}$$

$$d=C_{13}C_{55}-C_{15}C_{35}, \tag{10}$$

$$e=C_{13}C_{25}-C_{15}C_{23}, \tag{11}$$

$$\begin{aligned}f=\;&C_{11}(C_{22}C_{55}-C_{25}^2)-C_{12}(C_{12}C_{55}-C_{15}C_{25})\\&+C_{15}(C_{12}C_{25}-C_{15}C_{22})+C_{25}(C_{23}C_{35}-C_{25}C_{33}),\end{aligned} \tag{12}$$

$$\begin{aligned}\Omega=\;&2\big[C_{15}C_{25}(C_{33}C_{12}-C_{13}C_{23})+C_{15}C_{35}(C_{22}C_{13}\\&-C_{12}C_{23})+C_{25}C_{35}(C_{11}C_{23}-C_{12}C_{13})\big]\\&-\big[C_{15}^2(C_{33}C_{22}-C_{23}^2)+C_{25}^2(C_{33}C_{11}-C_{13}^2)\\&+C_{35}^2(C_{22}C_{11}-C_{12}^2)\big]+gC_{55},\end{aligned} \tag{13}$$

$$\begin{aligned}g=\;&C_{11}C_{22}C_{33}-C_{11}C_{23}^2-C_{22}C_{13}^2\\&-C_{33}C_{12}^2+2C_{12}C_{13}C_{23},\end{aligned} \tag{14}$$

$$B_{\rm V}=\frac{1}{9}[C_{11}+C_{22}+C_{33}+2(C_{12}+C_{13}+C_{23})], \tag{15}$$

$$\begin{aligned}G_V=\;&\frac{1}{15}[C_{11}+C_{22}+C_{33}+3(C_{44}+C_{55}+C_{66})\\&-(C_{12}+C_{13}+C_{23})].\end{aligned} \tag{16}$$

Here B, G, E, and ν represent the bulk modulus, shear modulus, Young's modulus, and Possion's ratio, respectively. The subscripts V, R, and H denote Voigt bound, Reuss bound, and Hill average, respectively. The arithmetic average of Voigt and Reuss bounds is termed as the Voigt–Reuss–Hill approximations.[28] Based on this method, Young's modulus E and Possion's ratio ν were derived from the following formulas:

$$E=9BG/(3B+G), \tag{17}$$

$$\nu=(3B-2G)/(3B+G)/2. \tag{18}$$

Furthermore, Young's modulus of VI_3 was projected on the ab and bc planes by using ELATE program.[29]

To investigate the thermal transport in VI_3, the harmonic interatomic force constants were calculated. We chose the

$2\times2\times2$ supercell with Γ-centered $1\times1\times1$ $\boldsymbol{k}$-mesh. In order to obtain the anharmonic interatomic force constants, a $2\times2\times2$ supercell with Γ-centered $1\times1\times1$ $\boldsymbol{k}$-mesh was chosen and up to the eight-nearest neighbors were considered. The thermal conductivity was calculated with the Sheng-BTE code[30] by iteratively solving the linearized BTE. A $11\times11\times5$ $\boldsymbol{q}$-mesh with a scalebroad of 1.0 for $R\bar{3}$ phase (a $11\times5\times11$ $\boldsymbol{q}$-mesh with a scalebroad of 1.0 for $C2/m$ phase) was chosen to guarantee the convergence of calculations. In order to describe phase transition effects on phonon–phonon scattering, the weighted phonon–phonon scattering phase space (WP3) was calculated and written as[31,32]

$$W_{\lambda}^{\pm}=\frac{1}{2N}\sum_{\lambda'\lambda''}\left\{\begin{array}{c}2(f_{\lambda'}-f_{\lambda''})\\ f_{\lambda'}+f_{\lambda''}+1\end{array}\right\}\frac{\delta(\omega_{\lambda}\pm\omega_{\lambda'}-\omega_{\lambda''})}{\omega_{\lambda}\omega_{\lambda'}\omega_{\lambda''}},\quad(19)$$

where N is the number of phonon modes λ including phonon wavevector and branch, f_{λ} is the equilibrium phonon distribution, and ω is the phonon angular frequency. The phonon mode λ'' is determined under the condition of quasi-momentum conservation $\lambda''=\lambda\pm\lambda'+p$, where p is the reciprocal lattice vector and the symbol "$\pm$" means the adsorption $(+)$ and emission $(-)$ processes.

In order to clearly show the difference of phonon lifetime between $C2/m$ and $R\bar{3}$ phases, the average value $(\bar{\tau}\,)$ was evaluated as[33]

$$\bar{\tau}=\frac{\int(v_{\lambda}^{\alpha}(\omega_{\lambda}))^{2}C(\omega_{\lambda})\tau(\omega_{\lambda})\mathrm{d}\omega}{\int C(\omega_{\lambda})(v_{\lambda}^{\alpha}(\omega_{\lambda}))^{2}\mathrm{d}\omega},\quad(20)$$

where $\mathrm{DOS}(\omega_{\lambda})$ is the phonon density of states, $C(\omega_{\lambda})$ and $\tau(\omega_{\lambda})$ are the specific heat and phonon lifetime of mode λ, respectively.

3. Results and discussion

The high-temperature crystal structure of VI_3 is monoclinic $AlCl_3$ structural type (space group $C2/m$, No. 12) with V^{3+} cations surrounded by six I^- anions in an octahedral coordination as shown in Figs. 1(a) and 1(b). When the temperature is below 79 K, VI_3 adopts the rhombohedral BiI_3 structural type (space group $R\bar{3}$, No. 148) as illustrated in Figs. 1(c) and 1(d). Each layer in both two structure types is stacked along c-axis via vdW interaction. The lattice constants and interlayer spacing of the two structures are summarized in Table 1. The interlayer spacing contracts 2.9% with the structural transition from monoclinic phase to rhombohedral one. Such a huge change of interlayer spacing has also been observed in other layered magnetic halide compounds and it could be attributed to the spin–lattice coupling. The effect of spin polarization or FM ordering on structural stability will be discussed below. Moreover, from Fig. 1(b), V and I atoms show different configurations along the a- and b-axis in monoclinic phase, indicating the anisotropy within the in-plane directions; while these atoms display the same configurations within the in-plane directions in the rhombohedral phase as shown in Fig. 1(d). Hence, the thermal properties of VI_3 should undergo a transition from anisotropy to isotropy within the in-plane directions when the phase transition occurs from monoclinic structure to rhombohedral one.

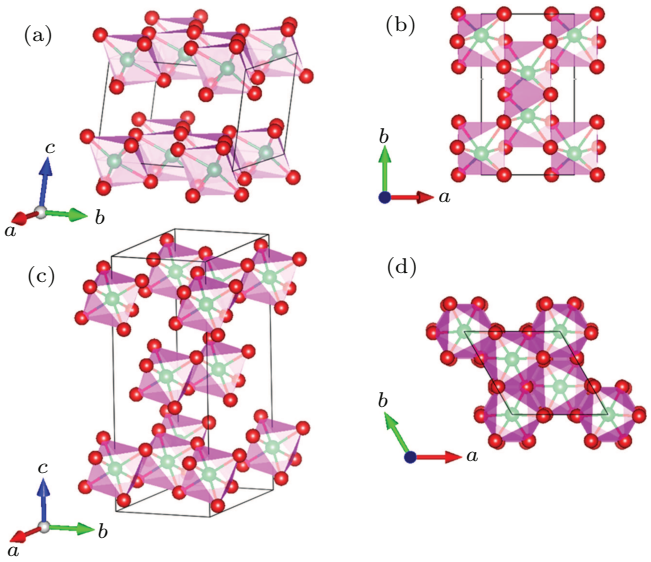


Fig. 1. The atomic structure of VI_3 with monoclinic phase (a), (b) and rhombohedral phase (c), (d). The V atoms are in olive green and the I atoms are in red.

Table 1. Lattice constants a, b, and c (nm), layer spacing (nm), bulk modulus B (GPa), shear modulus G (GPa), Young's modulus E (GPa), and Possion's ratio ν for VI_3 in monoclinic and rhombohedral phases.

Phase	a	b	c	Layer spacing	B	G	E	ν
$C2/m$	0.6818	1.1225	0.7151	0.6821	20	13	32	0.22
$R\bar{3}$	0.6961	0.6961	1.9878	0.6624	14.6	9.4	23	0.24

First, the dynamic stabilities of VI_3 with different phases are investigated by comparing their phonon dispersions (Fig. 3). Based on the experimental data, VI_3 exhibits monoclinic structure without long-range ferromagnetic ordering when the temperature is higher than 79 K, so the spin polarization is switched off in our first-principles calculations when mimicking phonon transport in monoclinic phase of VI_3. Because the long-range ferromagnetic ordering appears for VI_3 when the temperature is lower than 50 K and the intermediate state between 79 K and 50 K might be complex, in the current work we focus on the thermal switching before and after the phase transition rather than the complex phase transition process and $R\bar{3}$ phase is considered when the temperature is lower than 50 K. The phonon dispersions of $R\bar{3}$ structure are calculated with and without spin polarization. Compared to the phonon dispersion of NM $R\bar{3}$ shown in Fig. 2(c), the imaginary frequency disappears in FM $R\bar{3}$ as shown in Fig. 2(a). Thus, for $R\bar{3}$ phase, FM phase is the ground state. As discussed above, there is no long-range ferromagnetic ordering for $C2/m$ structure and its phonon dispersion with NM phase as shown in Fig. 2(b) has no imaginary frequency, indicating that the high-temperature structure prefers to monoclinic

NM $C2/m$ phase, which is consist with Tian's findings.[19] Therefore, NM $C2/m$ and FM $R\bar{3}$ are considered as the low-temperature and high-temperature phases of VI_3, respectively in this work. The primitive cell of $C2/m$ structure contains 16 atoms so that the phonon spectrum of this phase has 48 branches; while the primitive cell of $R\bar{3}$ structure contains 24 atoms, 24 more branches exist in its phonon spectrum, leading to more scattering channels in $R\bar{3}$ structure. It is obvious that the optical branches shift to lower frequency region in $R\bar{3}$ structure. This is also seen from the phonon density of states in Fig. 2(d) that overall phonon modes of $R\bar{3}$ structure are softening throughout the Brillouin zone. This redshift of lower optical branches or phonon softening indicates that the $C2/m$ structure is stiffer than the $R\bar{3}$ structure.

As discussed above, the $C2/m$ structure is stiffer than the $R\bar{3}$ structure. Then, the elastic properties of the two structures are calculated based on their elastic modulus tensors.

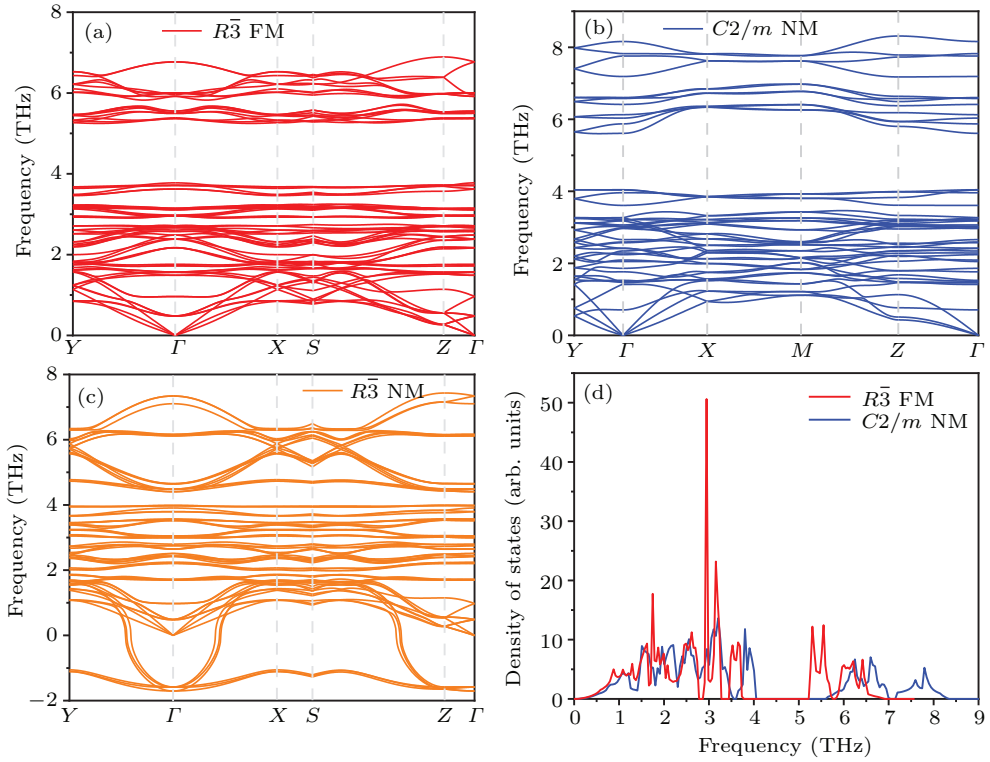


Fig. 2. Phonon dispersion of VI_3 with ferromagnetic $R\bar{3}$ structure (a), with nonmagnetic $C2/m$ structure (b) and nonmagnetic $R\bar{3}$ structure (c). (d) Phonon density of states in VI_3 with ferromagnetic $R\bar{3}$ structure (red line) and nonmagnetic $C2/m$ structure (blue line).

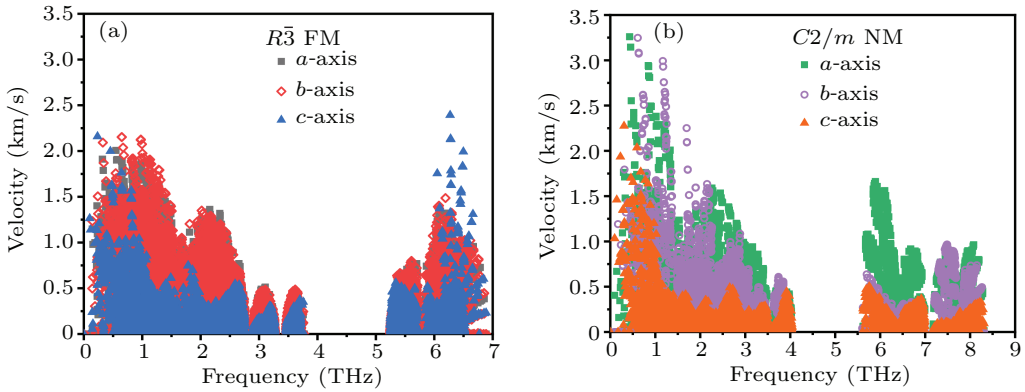


Fig. 3. Phonon group velocity of VI_3 with FM $R\bar{3}$ phase (a) and NM $C2/m$ phase (b) along different axis.

The elastic modulus tensor C_{ij} is obtained from the stress–strain relationship as $\sigma = C_{ij}\varepsilon$, where σ and ε are the engineering stress and strain vector, respectively.[8,34] Based on the elastic modulus tensor, the mechanical properties such as Young's modulus of $C2/m$ and $R\bar{3}$ structures are calculated.[27,35] Due to the different space groups of the two structures, different equations listed in Section 2 are employed. The calculated results are summarized in Table 1. In detail, Young's moduli of $C2/m$ phase is 39.1% larger than that of $R\bar{3}$ one. Meanwhile, Young's modulus of VI_3 in both phases are also larger than that of nine-layers thick CrI_3 with the value of 15 GPa,[36] which means VI_3 can sustain more strains

than CrI_3. Larger Young's modulus represents stiffer structure which leads to larger phonon velocity. So, it is clear that the highest phonon velocities of $C2/m$ within the in-plane direction are larger than that of $R\bar{3}$ as shown in Fig. 3. Such a phenomenon can also be reflected in the directional dependence of Young's modulus in the *ab* plane of the two phases as shown in Fig. 4. For $R\bar{3}$ phase, the same Young's modulus within the in-plane directions manifests the isotropic mechanical properties in the *ab* plane. For $C2/m$ phase, Young's modulus along the *a*-axis is almost 1.65 times that of $R\bar{3}$ phase. Thus, $C2/m$ phase exhibits anisotropic mechanical properties, which leads to its anisotropic thermal conductivity. Especially, Young's moduli of both phases along the out-of-plane direction are the smallest due to the weak vdW interactions, which is also reflected in the thermal properties. Besides the difference of Young's moduli of the two phases, the smaller Poisson's ratio of 0.22 for $C2/m$ structure (0.24 for $R\bar{3}$ structure) indicates that the bonding is more directional in $C2/m$ structure.[37] The V–I bond distance of 2.757 Å is uniform in $R\bar{3}$ structure, while the V–I bonds display two lengthes of 2.712 Å and 2.908 Å in $C2/m$ structure. This also implies the anisotropy of $C2/m$ structure. On the other hand, the ratio of bulk modulus (B) and shear modulus (G) of $R\bar{3}$ structure is larger than that of $C2/m$ structure, indicating larger ductility of $C2/m$ phase.[37,38]

In order to investigate the thermal switching of VI_3 from $C2/m$ to $R\bar{3}$ phase, the lattice thermal conductivities of the two phases are calculated based on Boltzmann transport equation and the calculated results are shown in Fig. 5(a). When temperature is lower than 50 K, the thermal conductivities of $R\bar{3}$ VI_3 have the same values along *a*-axis and *b*-axis directions; while the thermal conductivities become different along *a*-axis and *b*-axis directions when the phase transforms from $R\bar{3}$ to $C2/m$ at the transition temperature. These results clearly demonstrate the isotropic property of $R\bar{3}$ phase within the in-plane direction and anisotropic property of $C2/m$ phase. Meanwhile, the thermal conductivity of $C2/m$ phase is much larger than that of $R\bar{3}$ phase for all three directions. Quantitatively, at the phase transition temperature, the largest switching ratio can reach to 3.9 along the *a*-axis, which is much larger than that predicted in bulk FeRh of 1.4[39] and semi-hydrogenated graphene of 2.3.[40]

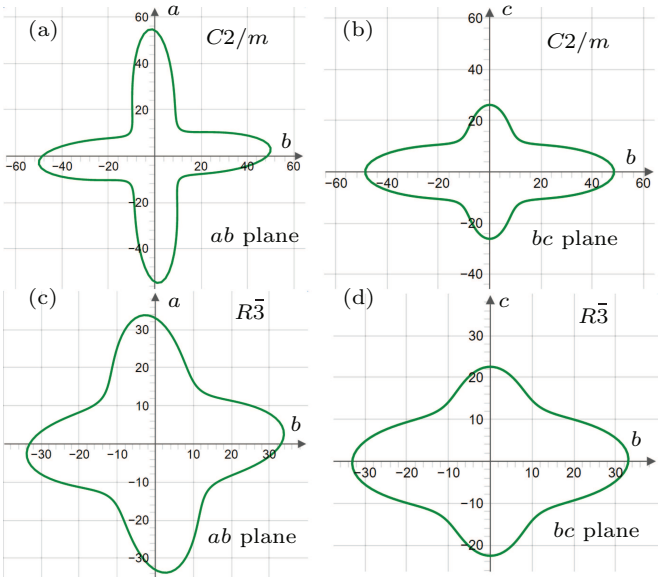


Fig. 4. Directional dependence of Young's modulus projected into the *ab* plane of $C2/m$ phase (a), (b) and $R\bar{3}$ phase (c), (d).

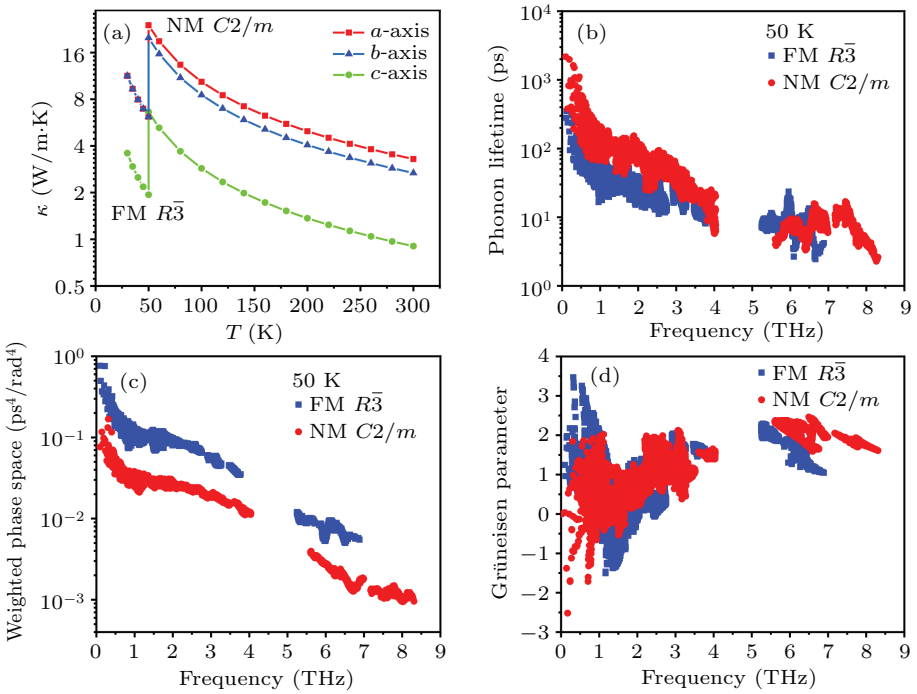


Fig. 5. (a) Lattice thermal conductivity of VI_3 with FM $R\bar{3}$ and NM $C2/m$ phases as a function of temperature. The frequency-dependent phonon lifetime (b), weighted phonon–phonon scattering phase space (c) and Grüneisen parameters (d) of VI_3 with FM $R\bar{3}$ (blue squares) and NM $C2/m$ (red circles) phases. Notably, the phonon lifetime and WP3 are obtained at 50 K.

As mentioned above, the narrowed phonon band gap of phonon branches provides more channels for phonon–phonon scattering, leading to the decrease in phonon lifetime. From Fig. 5(b), the phonon lifetime of $R\bar{3}$ phase is actually shorter than that of $C2/m$ phase. The average lifetime in $R\bar{3}$ phase is 28 ps, while in $C2/m$ phase it is 74 ps. The 2.6 times increase in lifetime is consistent with the 3.9 times increase in thermal conductivity, indicating the dominant effects of phonon lifetime on the thermal switching. To further understand the reason for increase in phonon lifetime, we analyze the phonon–phonon scattering phase space and phonon anharmonicity. The frequency dependent weighted phonon–phonon scattering phase space WP3[41] and Grüneisen parameters, indicators of phonon anharmonicity, are then calculated. It is clearly that the WP3 of $R\bar{3}$ phase is much larger than that of $C2/m$ phase, indicating more phonon scattering channels in $R\bar{3}$ structure. To quantify the WP3, the specific heat averaged value is calculated and they are 0.08 ps^4/rad^4 and 0.02 ps^4/rad^4 for FM $R\bar{3}$ and NM $C2/m$, respectively. However, the calculated average Grüneisen parameters at 50 K are 0.6 and 0.9 for FM $R\bar{3}$ and NM $C2/m$, respectively, implying that $R\bar{3}$ structure has weaker lattice anharmonicity, inconsistent with the shorter phonon lifetime. The larger phonon anharmonicity in cubic phase has also been found in III–V and II–VI semiconductors with cubic and hexagonal phases.[42] The weaker lattice anharmonicity in $R\bar{3}$ structure can be explained by ferromagnetic ordering caused attenuation of anharmonicity in $R\bar{3}$ structure. It has also been reported in CrI_3[43] and semi-hydrogenated graphene.[40] Therefore, the reduced WP3 is the main factor for the enhancement of phonon lifetime in $C2/m$ phase.

4. Conclusion

In summary, this work initially focuses on the dynamic stability of different phases of VI_3 with or without spin polarization. The calculated results indicate that the $R\bar{3}$ phase with ferromagnetic ordering is dynamically stable and the high-temperature structure of VI_3 prefers to $C2/m$ phase. With the further investigations on mechanical properties of both phases, Young's modulus of $C2/m$ phase is 33% larger than that of $R\bar{3}$ phase, implying the higher phonon group velocity in $C2/m$ phase. Moreover, the phonon lifetime decreases by 2.6 times as the structure transforms from $C2/m$ to $R\bar{3}$ phase. This drop is attributed to the increase of phonon–phonon scattering channels in $R\bar{3}$ phase. The variations of phonon lifetime and group velocity at the phase transition from $C2/m$ to $R\bar{3}$ cause the large thermal switching ratio of 3.9 in VI_3. This reversible thermal conductivity enables us to control thermal energy in magnetic materials-based devices.

Data availability statement

The data that support the findings of this study are available from the corresponding author upon reasonable request.

Acknowledgements

Project supported by the National Natural Science Foundation of China (Grant No. 52206092) and the Natural Science Foundation of Jiangsu Province, China (Grant No. BK20210565). C. Liu was funded by Department of Science and Technology of Jiangsu Province, China (Grant No. BK20220032), Basic Science (Natural Science) Research Project of Higher Education Institutions of Jiangsu Province, China (Grant No. 21KJB470009), and Nanjing Science and Technology Innovation Project for Overseas Students. C. Liu was also funded by "Shuangchuang" Doctor Program of Jiangsu Province, China (Grant No. JSSCBS20210315) and open research fund of Jiangsu Key Laboratory for Design and Manufacture of Micro-Nano Biomedical Instruments, Southeast University (Grant No. KF202010). The authors thank the Scientific Computing Center of Nanjing Normal University and the Big Data Center of Southeast University for performing the numerical calculations presented in this paper.

References

[1] Aryana K, Tomko J A, Gao R, Hoglund E R, Mimura T, Makarem S, Salanova A, Hoque M S B, Pfeifer T W, Olson D H, Braun J L, Nag J, Read J C, Howe J M, Opila E J, Martin L W, Ihlefeld J F and Hopkins P E 2022 *Nat. Commun.* **13** 1573
[2] Du T, Xiong Z, Delgado L, Liao W, Peoples J, Kantharaj R, Chowdhury P R, Marconnet A and Ruan X 2021 *Nat. Commun.* **12** 4915
[3] Tomko J A, Pena-Francesch A, Jung H, Tyagi M, Allen B D, Demirel M C and Hopkins P E 2018 *Nat. Nanotech.* **13** 959
[4] Liu C and Chen Y 2022 *Sci. China-Phys. Mech. Astron.* **65** 117009
[5] Wehmeyer G, Yabuki T, Monachon C, Wu J and Dames C 2017 *Appl. Phys. Rev.* **4** 041304
[6] Liu C, Mishra V, Chen Y and Dames C 2018 *Adv. Theor. Simul.* **1** 1800098
[7] Liu C, Lu P, Gu Z Z, Yang J and Chen Y 2020 *J. Phys. Chem. C* **124** 26144
[8] Wang Y and Ren J 2021 *ACS Appl. Mater. Interfaces* **13** 34724
[9] Liu Y, Liu Q, Liu Y, Jiang X, Zhang X and Zhao J 2021 *Nanoscale* **13** 7714
[10] Liu C, Si W, Wu C, Yang J, Chen Y and Dames C 2020 *Acta Mater.* **191** 221
[11] Zhang W, Chen W Z and Jiang Z Y 2012 *Acta Phys. Sin.* **61** 148105 (in Chinese)
[12] Cocemasov A I, Isacova C I and Nika D L 2018 *Chin. Phys. B* **27** 056301
[13] Ihlefeld J F, Foley B M, Scrymgeour D A, Michael J R, McKenzie B B, Medlin D L, Wallace M, Trolier-McKinstry S and Hopkins P E 2015 *Nano Lett.* **15** 1791
[14] Liu H, Shi X, Xu F, Zhang L, Zhang W, Chen L, Li Q, Uher C, Day T and Snyder G J 2012 *Nat. Mater.* **11** 422
[15] Shrestha R, Luan Y, Shin S, Zhang T, Luo X, Lundh J S, Gong W, Bockstaller M R, Choi S, Luo T, Chen R, Hippalgaonkar K and Shen S 2019 *Sci. Adv.* **5** eaax3777
[16] Lu Q, Huberman S, Zhang H, Song Q, Wang J, Vardar G, Hunt A, Waluyo I, Chen G and Yildiz B 2020 *Nat. Mater.* **19** 655
[17] Liu C, Chen Z, Wu C, Qi J, Hao M, Lu P and Chen Y 2022 *ACS Appl. Mater. Interfaces* **14** 46716

[18] Lyu B B, Gao Y F, Zhang Y, Wang L, Wu X, Chen Y, Zhang J, Li G, Huang Q, Zhang N, Chen Y, Mei J, Yan H, Zhao Y, Huang L and Huang M 2020 *Nano Lett.* **20** 6024

[19] Tian S, Zhang J F, Li C, Ying T, Li S, Zhang X, Liu K and Lei H 2019 *J. Am. Chem. Soc.* **141** 5326

[20] Kong T, Stolze K, Timmons E I, Tao J, Ni D, Guo S, Yang Z, Prozorov R and Cava R J 2019 *Adv. Mater.* **31** 1808074

[21] Kheirkhah M, Yan Z, Nagai Y and Marsiglio F 2020 *Phys. Rev. Lett.* **125** 017001

[22] Guin S N, Banerjee S, Sanyal D, Pati S K and Biswas K 2017 *Chem. Mater.* **29** 3769

[23] Perdew J P, Burke K and Ernzerhof M 1996 *Phys. Rev. Lett.* **77** 3865

[24] Grimme S, Antony J, Ehrlich S and Krieg H 2010 *J. Chem. Phys.* **132** 154104

[25] Dingreville R and Qu J 2005 *J. Mech. Phys. Solids* **53** 1827

[26] Watt J P 1980 *J. Appl. Phys.* **51** 1520

[27] Azzouz L, Halit M, Sidoumou M, Charifi Z, Allal A, Bouchenafa M and Baaziz H 2019 *Phys. Status Solidi B* **256** 1900136

[28] Chung D H and Buessem W R 1967 *J. Appl. Phys.* **38** 2535

[29] Gaillac R, Pullumbi P and Coudert F X 2016 *J. Phys. Condens. Matter* **28** 275201

[30] Li W, Carrete J, A. Katcho N and Mingo N 2014 *Comput. Phys. Commun.* **185** 1747

[31] Li W and Mingo N 2014 *Phys. Rev. B* **89** 184304

[32] Li W and Mingo N 2015 *Phys. Rev. B* **91** 144304

[33] Torres P, Torelló A, Bafaluy J, Camacho J, Cartoixà X and Alvarez F X 2017 *Phys. Rev. B* **95** 165407

[34] Xiao Y, Chang C, Pei Y, Wu D, Peng K, Zhou X, Gong S, He J, Zhang Y, Zeng Z and Zhao L D 2016 *Phys. Rev. B* **94** 125203

[35] Hill R 1952 *Proc. Phys. Soc. Sect. A* **65** 349

[36] Cantos-Prieto F, Falin A, Alliati M, Qian D, Zhang R, Tao T, Barnett M R, Santos E J G, Li L H and Navarro-Moratalla E 2021 *Nano Lett.* **21** 3379

[37] Wu Z J, Zhao E J, Xiang H P, Hao X F, Liu X J and Meng J 2007 *Phys. Rev. B* **76** 054115

[38] Liu H, Tang S, Ma Y, Liu W and Liang C 2021 *Scripta Mater.* **204** 114136

[39] Cazorla C and Rurali R 2022 *Phys. Rev. B* **105** 104401

[40] Li H, Zhang P, Ouyang T, Wang H, Li J, He C, Zhang C and Tang C 2022 *Appl. Phys. Lett.* **120** 092403

[41] Wang Z, Zhang T, Ding M, Dong B, Li Y, Chen M, Li X, Huang J, Wang H, Zhao X, Li Y, Li D, Jia C, Sun L, Guo H, Ye Y, Sun D, Chen Y, Yang T, Zhang J, Ono S, Han Z and Zhang Z 2018 *Nat. Nanotech.* **13** 554

[42] Raya-Moreno M, Rurali R and Cartoixà X 2019 *Phys. Rev. Mater.* **3** 084607

[43] Qin G, Wang H, Zhang L, Qin Z and Hu M 2020 *J. Mater. Chem. C* **8** 3520